MEG-Based Imaging of Focal Neuronal Current Sources

James W. Phillips, *Member, IEEE*, Richard M. Leahy,* *Member, IEEE*, and John C. Mosher, *Member, IEEE*

***Abstract*— We describe a new approach to imaging neural current sources from measurements of the magnetoencephalogram (MEG) associated with sensory, motor, or cognitive brain activation. Many previous approaches to this problem have concentrated on the use of weighted minimum norm (WMN) inverse methods. While these methods ensure a unique solution, they do not introduce information specific to the MEG inverse problem, often producing overly smoothed solutions and exhibiting severe sensitivity to noise. We describe a Bayesian formulation of the inverse problem in which a Gibbs prior is constructed to reflect the sparse focal nature of neural current sources associated with evoked response data. We demonstrate the method with simulated and experimental phantom data, comparing its performance with several WMN methods.**

***Index Terms*— Bayesian imaging, magnetoencephalogram, mean field annealing, minimum norm.**

I. Introduction

MEASUREMENTS of the magnetic field produced by electrical brain activity can be made using an array of superconducting quantum interference device (SQUID) biomagnetometers. These measurements of the magnetoencephalogram (MEG), and the associated scalp potentials or electroencephalogram (EEG), are able to follow changes in neural activity on a millisecond time scale and provide unique insights into the dynamic behavior of the human brain. In comparison, the other functional neuroimaging modalities [functional magnetic resonance imaging (fMRI), and single-photon and positron emission computed tomography (SPECT and PET)] are limited to temporal resolutions on the order of, at best, one second, due to physiological time constants and signal-to-noise considerations. Furthermore, MEG signals are produced directly by the electrical activity through which the brain communicates, rather than the indirect correlates, such as regional cerebral blood flow or glucose metabolism, that are imaged by the alternative functional modalities.

To produce estimates of the neural current sources that generate the observed MEG signal, we must solve the associated quasi-static electromagnetic inverse problem. The inherent ill-posedness of this problem, compounded by the limited number of spatial measurements available with current MEG systems, presents a difficult challenge for standard methods of image reconstruction. In the following we will describe an alternative Bayesian approach that uses a physiologically based model for the source to estimate a plausible solution from the available data.

Physiological models for event related MEG assume that the dominant sources are transmembrane and intracellular currents in the apical dendrites of the cortical pyramidal cells [1]. The source image can, therefore, be constrained to the cortex, which can be extracted from a registered volume magnetic resonance (MR) image of the subject's head. Furthermore, the orientation of these cells normal to the cortical surface allows us to constrain the orientation of the cortical current sources [1].

By tessellating the cortex with N disjoint regions and representing the sources in each region by an equivalent constrained current dipole [2] oriented normal to the surface with amplitude y_i, the MEG inverse problem can be expressed in terms of a linear model. The linear forward model relating the N sources $\mathbf{y}(N \times 1)$ and the M MEG measurements $\mathbf{b}(M \times 1)$ can be written

$$\mathbf{b} = \mathbf{G}\mathbf{y} + \mathbf{n} \tag{1}$$

where the ith row of the $M \times N$ system matrix $\mathbf{G}$ may be viewed as a discrete constrained projection of the lead field (sensitivity) of the ith sensor. The jth column of $\mathbf{G}$ specifies the gain vector for the jth constrained dipole component. The $M \times 1$ vector $\mathbf{n}$ represents noise generated within the sensor and by unwanted electromagnetic sources (power lines, the heart, background brain activity, etc.), or from modeling errors.

We use a quasi-static approximation, since the time derivatives of the electric and magnetic field are small compared to the ohmic current [3]. If the head is modeled as a spherically symmetric conductor, the radial component of the magnetic field outside the head is entirely due to the primary current; consideration of the volume or return currents can be neglected. In this case, the relationship between the jth source dipole and the radial magnetometer measurement at the ith

Manuscript received January 25, 1996; revised October 5, 1996. This work was supported by the National Institute of Mental Health under Grant R01-MH53213, the National Eye Institute under Grant R01-EY08610, and the Los Alamos National Laboratory, operated by the University of California for the U. S. Department of Energy, under Contract W-7405-ENG-36. The Associate Editor responsible for coordinating the review of this paper and recommending its publication was Y. Censor. *Asterisk indicates corresponding author.*

J. W. Phillips is with the Signal and Image Processing Institute, University of Southern California, Los Angeles, CA 90089 USA (e-mail: jamesphi@sipi.usc.edu).

*R. M. Leahy is with the Signal and Image Processing Institute, University of Southern California, 3740 McClintock Ave., Los Angeles, CA 90089 USA (e-mail: leahy@sipi.usc.edu).

J. C. Mosher is with Los Alamos National Laboratory, Los Alamos, NM 87545 USA. (e-mail: mosher@LANL.Gov).

Publisher Item Identifier S 0278-0062(97)03954-2.

sensor is [4]

$$g_{ij} = \frac{\mu_0}{4\pi} \frac{\mathbf{r}_i \times \mathbf{l}_j}{|\mathbf{r}_i - \mathbf{l}_j|^3 |\mathbf{r}_i|} \cdot \mathbf{e}_j \tag{2}$$

where μ_0 is the permittivity of free space, $\mathbf{l}_j$ and $\mathbf{r}_i$ are the locations of the dipole j and sensor i, respectively, and $\mathbf{e}_j$ is a unit magnitude vector for the orientation of the jth constrained source.

In practice, of course, the head is not spherical and the sensors do not make point measurements of the radial component of the magnetic field. To reduce sensitivity to distant sources and the earth's magnetic field, a gradiometer is used to measure the difference in the magnetic flux through two adjacent coils. The forward model is easily modified to include the effects of the gradiometer and of nonradial sensors [4], [5]. Finite and boundary element methods can be used to further extend the model to include nonspherical head geometries (cf. [6]). While the forward model in these cases becomes increasingly complex, the problem remains linear and the reconstruction methods described below can still be used. In the experimental results presented below we use a spherical head geometry but specifically model the nonradial, planar gradiometer configuration of the Neuromag122 MEG system used in our work [4], [7].

A linear relationship also exists between the primary current density and the potential difference between two electrodes measured by the EEG. Mosher *et al.* [8] and Cuffin and Cohen [9] show quantitatively that MEG and EEG provide complementary information. In the spherical head model, MEG is sensitive only to the tangential component of the primary current density, whereas EEG is sensitive to all components, and the MEG lead field magnitude falls off more quickly than EEG near the center of the sphere. However, EEG is more sensitive to uncertainties in the head model. To obtain the best conditioned data set, therefore, simultaneous EEG and MEG data can be acquired and used to reconstruct the current source distribution. In the following, we will concentrate on MEG only.

Most inverse procedures for EEG/MEG can be classified as either multiple dipole or imaging methods. Multiple dipole methods assume that a small set of current dipoles can adequately represent the unknown source distribution. The dipole locations and moments form a set of unknown parameters which are typically found using a nonlinear least squares fit to the observed data [10], [11]. Scherg and von Cramon [12] extended the least squares approach to utilize the full spatio-temporal data by constraining the dipole locations to be fixed for the duration of the measured response. The error surface is highly nonconvex with respect to the location parameters. The multiple signal classification (MUSIC) algorithm [13] avoids some of the problems due to this nonconvexity through the use of signal subspace techniques [14]. While multiple dipole methods are ideal for point sources, they may perform poorly if sources are distributed and nondipolar over a significant area. Multipole expansions can be used to represent these more distributed sources [15], but this approach has received little recent attention in the EEG and MEG literature. Imaging is also well suited for distributed source representation, with the advantage that the inverse problem is linear in the source intensities and that anatomical constraints can be easily introduced.

The major disadvantage of the imaging approach over multiple dipole methods is that the number of unknowns can rise dramatically and the problem is typically highly underdetermined. The search for an appropriate imaging method is primarily concerned with finding a way to choose within a set of images that produces essentially the same fit to the data. Weighted minimum norm inverse methods [4], [7], [16], [17] typically find solutions which match the data while minimizing a weighted l_2 norm on the solution vector. These techniques tend to smear sources over the entire reconstruction region and are generally unstable due to ill-conditioning of the system matrix. The instability can be overcome using Tikhonov regularization [18] but the reconstructions remain smeared.

The iteratively reweighted minimum norm method [19], [20] is a nonlinear approach to overcoming the problem of smeared sources in which the norm weighting is updated at each iteration based on the result of the previous iteration. This method uses a weighting matrix which, as the iterations proceed, reinforces strong sources and reduces weak ones. This results in very sparse solutions, but again the method is extremely sensitive to noise and highly dependent on the initial estimate. Leahy and Jeffs [21], [22] examined minimization of the l_P norm of the solution vector, for $P \leq 1$, subject to linear inequality constraints on the data. They show that there exist values of $P \leq 1$ for which the resulting solution is maximally sparse. Later, Matsuura *et al.* [23], [24] reexamined the linear programming case ($P = 1$), which they refer to as the selective minimum norm approach, and showed examples of sparse solutions obtained using linear inequality constraints.

Here, we propose an alternative approach to the inverse problem based on a Bayesian formulation. Rather than use an arbitrary weighted l_P norm to select the solution, we introduce a prior distribution on the source which is used to resolve the ambiguities inherent in the inverse problem. This prior is constructed to favor the reconstruction of physiologically plausible solutions. Basic studies of functional activation, such as somatotopic or retinotopic mapping using fMRI or PET, reveal the sparse and highly localized nature of activation in the cerebral cortex [25]. Our prior is, therefore, specifically designed to reflect the expectation that current sources tend to be sparse and focal. This prior is combined with a Gaussian likelihood model for the data which is based on the linear model (1) and an assumption of additive white Gaussian noise. Maximization over the resulting posterior probability results in a maximum *a posteriori* (MAP) estimate of the primary current sources. In the following, we briefly describe the regularized, weighted minimum norm (WMN) methods. We then develop our Bayesian approach and describe a numerical procedure for computing a MAP image estimate. We compare the performance of the different methods for simulated data and experimental phantom data from a clinical Neuromag 122 channel MEG system.

II. Minimum l_2-Norm Approaches

The weighted minimum l_2-norm approach to linear inverse problems involves solving the constrained optimization problem

$$\mathbf{y}_{\text{wmn}} = \underset{\mathbf{y}}{\arg\min}\, \mathbf{y}^{\text{T}}\mathbf{C}_{\text{y}}^{-1}\mathbf{y} \quad \text{such that} \quad ||\mathbf{b}-\mathbf{G}\mathbf{y}||^2 = 0 \tag{3}$$

where $\mathbf{C}_{\text{y}}$ is an arbitrary symmetric positive definite matrix. Writing the Cholesky decomposition $\mathbf{C}_{\text{y}} = \mathbf{W}\mathbf{W}^{\text{T}}$, we can form the solution as

$$\mathbf{y}_{\text{wmn}} = \mathbf{W}\mathbf{W}^{\text{T}}\mathbf{G}^{\text{T}}(\mathbf{G}\mathbf{W}\mathbf{W}^{\text{T}}\mathbf{G}^{\text{T}})^{-1}\mathbf{b} = \mathbf{W}(\mathbf{G}\mathbf{W})^{\dagger}\mathbf{b} \tag{4}$$

where $(\mathbf{G}\mathbf{W})^{\dagger}$ denotes the pseudoinverse of $\mathbf{G}\mathbf{W}$. The WMN solution can also be formed from the singular value decomposition (SVD) of $\mathbf{G}\mathbf{W}$

$$\mathbf{y}_{\text{wmn}} = \mathbf{W}\sum_{i=1}^{M}(\frac{\mathbf{u}_i^{\text{T}}\mathbf{b}}{s_i})\mathbf{v}_i \tag{5}$$

where s_i, $\mathbf{v}_i$, and $\mathbf{u}_i$ are the ith singular value and corresponding right and left singular vectors of $\mathbf{G}\mathbf{W}$, respectively.

Several forms of $\mathbf{W}$ have been proposed for MEG imaging applications. In [4] and [17], the weight matrix is implicitly the identity matrix ($\mathbf{W} = \mathbf{I}$). In the normalized minimum norm method [19], [26], $\mathbf{W}_{\text{norm}} = \text{diag}(1/||\mathbf{g}_1||, 1/||\mathbf{g}_2||, \cdots, 1/||\mathbf{g}_1||)$ where $||\mathbf{g}_i||$ is the Euclidean norm of the ith column of $\mathbf{G}$. This weighting is designed to compensate for the reduced sensitivity of MEG to deep sources which results in a preference for superficial distributions when $\mathbf{W} = \mathbf{I}$. The $N \times N$ Laplacian operator $\mathbf{B}$ may be selected to smooth the reconstruction of minimum norm techniques using $\mathbf{W} = \mathbf{B}^{-1}$ [27]. The low-resolution brain electromagnetic tomography (LORETA) technique [16] uses a combination of column normalization and the Lapacian operator $\mathbf{W}_{\text{L}} = \mathbf{W}_{\text{norm}}\mathbf{B}^{-1}$. Dale and Sereno [28] use a weighting based on estimates of signal power at each location. The signal power is estimated from the MEG data using a minimum variance array beamforming technique which may perform poorly for distributed or temporally dependent sources. If sources are independent and represented well by dipoles, however, the method has been shown to perform well empirically. They also introduce the possibility in [28] of making use of source location information extracted from other functional modalities.

Exact matching of the data in (3) results in ill-conditioning and high sensitivity to noise. Regularized forms of WMN methods lower this noise sensitivity. One popular technique is the truncated SVD [29] in which the summation in (5) is truncated at a threshold index. Tikhonov regularization [18] replaces the original problem (3) with the unconstrained minimization of a combination of the residual error norm and weighted l_2 norm of the solution vector

$$\mathbf{y}_{\lambda} = \underset{\mathbf{y}}{\arg\min}\, ||\mathbf{b}-\mathbf{G}\mathbf{y}||^2 + \lambda\mathbf{y}^{\text{T}}\mathbf{C}_{\text{y}}^{-1}\mathbf{y}. \tag{6}$$

For any value of the regularization parameter λ, the solution can be found as

$$\mathbf{y}_{\lambda} = \mathbf{W}\mathbf{W}^{\text{T}}\mathbf{G}^{\text{T}}(\mathbf{G}\mathbf{W}\mathbf{W}^{\text{T}}\mathbf{G}^{\text{T}} + \lambda\mathbf{I})^{-1}\mathbf{b} \tag{7}$$

$$= \mathbf{W}\sum_{i=1}^{M} f_i(\frac{\mathbf{u}_i^{\text{T}}\mathbf{b}}{s_i})\mathbf{v}_i \tag{8}$$

where the filter parameters are $f_i = s_i^2/(s_i^2+\lambda)$. Note that the filter coefficients decrease as s_i decreases. Therefore, the contributions of $(\mathbf{u}_i^{\text{T}}\mathbf{b}/s_i)\mathbf{v}_i$ to the solution from the smaller s_i are effectively filtered out. In our implementation of the regularized WMN methods we select an optimal value for λ using the L-curve method [18], [30].

The minimum norm methods can be reinterpreted in a Bayesian framework. Let $p(\mathbf{y})$ denote a prior probability on the unknown image $\mathbf{y}$, $p(\mathbf{b}|\mathbf{y})$ the probability of observing the data $\mathbf{b}$ given the source image $\mathbf{y}$, and $p(\mathbf{b})$ the probability of the observed data. Then, by Bayes' theorem, the posterior probability $p(\mathbf{y}|\mathbf{b})$ for the image $\mathbf{y}$ given the observed data $\mathbf{b}$ is

$$p(\mathbf{y}|\mathbf{b}) = \frac{p(\mathbf{b}|\mathbf{y})p(\mathbf{y})}{p(\mathbf{b})}. \tag{9}$$

While a general approach to image estimation using (9) involves the minimization of the expected value of an appropriately chosen loss function [31], in most image processing applications, the posterior probability is used to compute a MAP estimate

$$\mathbf{y}^* = \underset{\mathbf{y}}{\arg\max}\, \ln\{p(\mathbf{b}|\mathbf{y})\} + \ln\{p(\mathbf{y})\}. \tag{10}$$

If $\mathbf{y}$ and $\mathbf{n}$ are independent and normally distributed with zero mean and covariance $\mathbf{C}_{\text{y}}$ and $\mathbf{C}_{\text{n}}$, respectively, then the MAP estimate is

$$\mathbf{y}^* = \underset{\mathbf{y}}{\arg\max}\, \{-(\mathbf{G}\mathbf{y}-\mathbf{b})^{\text{T}}\mathbf{C}_{\text{n}}^{-1}(\mathbf{G}\mathbf{y}-\mathbf{b}) - \mathbf{y}^{\text{T}}\mathbf{C}_{\text{y}}^{-1}\mathbf{y}\}. \tag{11}$$

That is

$$\mathbf{y}^* = \mathbf{C}_{\text{y}}\mathbf{G}^{\text{T}}(\mathbf{G}\mathbf{C}_{\text{y}}\mathbf{G}^{\text{T}} + \mathbf{C}_{\text{n}})^{-1}\mathbf{b}. \tag{12}$$

For the noiseless case ($\mathbf{C}_{\text{n}} = \mathbf{0}$), this result is identical to (4), the WMN solution. Therefore, the various weight matrices can be interpreted in terms of the covariances of a Gaussian prior with $\mathbf{C}_{\text{y}} = \mathbf{W}\mathbf{W}^{\text{T}}$. If we assume $\mathbf{C}_{\text{n}} = \lambda\mathbf{I}$, we arrive at the general Tikhonov regularized form as given in (7) and (8).

This equivalence between regularized minimum norm methods and MAP image estimation is well known, see for example the discussions of Bayesian image estimation methods in [7], and [32]–[35]. If we view the WMN methods in this way, the choice of weight matrices are equivalent to a generally arbitrary selection of the covariance matrix of a Gaussian prior. The alternative formulation presented below replaces this arbitrary Gaussian prior with one chosen to better reflect the expected attributes of the current sources that produced the observed data.

III. Sparse Optimization

Since data from PET and fMRI show the sparse nature of neural activity, researchers have developed techniques to achieve a sparse image from the neuromagnetic data. In the WMN method of Dale and Sereno [28], sparse solutions are obtained by using a weighting function that favors the formation of sources at particular locations. While the method will perform well if the weightings are correctly specified, the problem of choosing where the sources should lie, i.e., choosing the weighting function, remains. Below, we briefly review other methods that do not require that the specific locations of the sparse sources be specified.

Leahy and Jeffs [21] describe a method for finding a solution vector to a set of linear inequality constraints that has the minimum number of nonzero elements. They show that under certain restrictions, this maximally sparse solution can be found by minimizing the l_P norm for all p in the range $0 \leq p \leq \alpha$ for some $0 < \alpha \leq 1$

$$\mathbf{y}_{p\text{norm}} = \arg\min_{\mathbf{y}} \sum_{i=1}^{N} |y_i|^p, \quad \text{such that} \quad |\mathbf{b} - \mathbf{G}\mathbf{y}| \leq \epsilon \tag{13}$$

where ϵ is a vector bounding the magnitude of the error in each data sample. The solution can be found using a modification of the simplex algorithm for linear programming. Matsuura *et al* [23], [24] also examine the linear programming simplex algorithm for MEG image reconstruction. In [24] an inequality constraint is used to bound the error on each measurement to $\pm\sigma_{\mathbf{n}}$ where $\sigma_{\mathbf{n}}$ is the standard deviation of the measurement noise. While this approach does lead to sparse solutions, placing a separate error bound on each measurement is undesirable for Gaussian noise, since we would expect a substantial number of the measurement errors to exceed $\pm\sigma_{\mathbf{n}}$.

An alternative approach to finding sparse solutions is a WMN method in which the weight matrix is iteratively updated using the result of the previous iteration. This method was originally investigated by Ioannides *et al.* [36], then more thoroughly developed by Gorodnitsky *et al.* [20]. The iteratively reweighted minimum norm approach, also known as focal underdetermined system solution (FOCUSS) [19], is a novel inverse method which first provides an initial estimate of $\mathbf{y}_0$ using (4) with $\mathbf{W}_{\text{norm}}$ as the weighting matrix. At each step thereafter, a new weight matrix $\mathbf{W}(k) = \text{diag}(\mathbf{y}(k-1))$ is formed. The solution is updated using

$$\mathbf{y}(k) = (\mathbf{W}_{\text{norm}}\mathbf{W}(k))(\mathbf{G}\mathbf{W}_{\text{norm}}\mathbf{W}(k))^{\dagger}\mathbf{b}. \tag{14}$$

For any starting point $\mathbf{y}(0)$, asymptotic convergence to a fixed point is guaranteed [20]. The fixed points are, however, unknown and highly dependent on the initial estimate. Also, the final error in fitting the data may be large, even for the noiseless case. In our implementation we use Tikhonov regularization with a fixed regularization parameter to avoid ill conditioning.

IV. The New Bayesian Approach

Since the primary sources of the MEG are widely accepted to be sparse and focal [25], [37], we suggest that this information be used in reconstructing the image. This information can be naturally introduced into the problem using the Bayesian paradigm in which the source is modeled as a random field. Since we assume that sources are sparse, the large majority of source pixels will have zero amplitude. We, therefore, use a binary indicator process $\mathbf{x}$ to model whether each source dipole is on ($x_i = 1$) or off ($x_i = 0$). Those sites that are active are assumed to have a Gaussian amplitude, z_i. We can then write the source image vector $\mathbf{y}$ as

$$\mathbf{y} = \mathbf{x}.*\mathbf{z} = \mathbf{X}\mathbf{z} \tag{15}$$

where ".*" signifies the Schur product (element by element pair-wise multiplication) and $\mathbf{X} = \text{diag}(\mathbf{x})$ is a diagonal matrix. Assuming independence of the indicator and amplitude processes, we can write the posterior probability for $\mathbf{x}$ and $\mathbf{z}$ given the MEG data $\mathbf{b}$ as

$$p(\mathbf{x}, \mathbf{z}|\mathbf{b}) = \frac{p(\mathbf{b}|\mathbf{x}, \mathbf{z})p(\mathbf{x})p(\mathbf{z})}{p(\mathbf{b})}. \tag{16}$$

We find a MAP estimate $\mathbf{y}^*$ of $\mathbf{y}$ as $\mathbf{y}^* = \mathbf{x}^*.*\mathbf{z}^*$ where

$$\mathbf{x}^*, \mathbf{z}^* = \arg\max_{\mathbf{x}, \mathbf{z}} \quad p(\mathbf{x}, \mathbf{z}|\mathbf{b}). \tag{17}$$

The joint probability $p(\mathbf{x})$ is chosen to reflect the expectation that the sources are sparse and focal. To achieve this goal, we use a Markov random field (MRF) [38] model for which sparse focal sources have a higher probability of occurring than more distributed sources. We define $p(\mathbf{x})$ to be a Gibbs distribution

$$p(\mathbf{x}) = (1/K)\exp\{-V(\mathbf{x})\} \tag{18}$$

where K is the partition function and the energy function $V(\mathbf{x})$ is given by

$$V(\mathbf{x}) = \sum_i \left[\underbrace{\alpha_i x_i}_{\text{Sparseness Term}} + \underbrace{\beta_i C_i\{x_i, x_j \; \forall \; j \in \xi_i\}}_{\text{Clustering Term}} \right] \tag{19}$$

where the parameters $\alpha_i > 0$ and $\beta_i > 0$ determine the relative weights of the sparseness and clustering terms. The potential function $C_i\{x_i, x_j \; \forall \; j \in \xi_i\}$ is defined in terms of each pixel and its eight nearest neighbors ξ_i as

$$C_i\{x_i, x_j \; \forall \; j \in \xi_i\} = \left[\sum_{j \in \xi_i} (x_i - x_j)^2 \right]^Q. \tag{20}$$

This clustering term is small if neighboring pixels are of the same magnitude. The exponential parameter Q determines the strength of the clustering. As Q increases, the size of the clusters tends to increase. Some examples of 2-D binary images produced by sampling from this prior using a Gibbs sampler [38], are shown in Fig. 1. Note that for $Q = 1$ the neighborhood consists of the eight nearest neighbors, but for $Q \neq 1$, this dilates to the nearest 24 neighbors since the

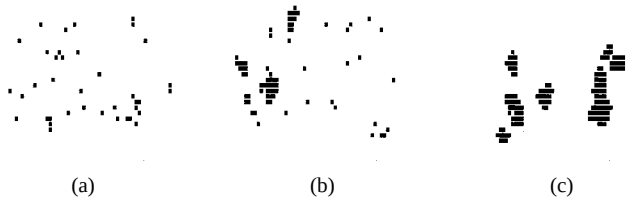

(a) (b) (c)

Fig. 1. Three examples of a random sampling from $p(\mathbf{x})$ on an annular segment reconstruction region. ξ_i is set as the pixel's nearest eight neighbors. (a) $Q = 1.0$, $\alpha = 0.20$, and $\beta = 0.25$ (b) $Q = 2.0$, $\alpha = 0.20$, and $\beta = 0.078$, and (c) $Q = 3.0$, $\alpha = 0.20$, and $\beta = 0.024$.

pairwise terms interactions become coupled when raised to any power $Q \neq 1$.

Since the parameters α_i determine the relative probabilities that each source pixel is active, it is straightforward to include pixel-wise probability weightings determined from fMRI or PET activation studies to influence the formation of these sparse images. However, here we assume no specific prior spatial information is available and we set $\alpha_i = \alpha$ and $\beta_i = \beta$ for all pixel sites i. The two characteristics of primary significance in choosing the parameters of the prior are the average number of active regions (clusters) and their average size. By qualitative inspection of images sampled from this prior we determined that $Q = 2.5$ gives acceptable control over the average number of clusters and cluster size by adjusting only the parameters α and β. We then used Markov Chain Monte Carlo methods to compute the average number of clusters and cluster size as a function of the parameters α and β. Mesh plots of the number of clusters in the image and the average cluster size are shown in Fig. 2.

To generate the values for these mesh plots, 2000 images were generated using a Gibb's sampler for each α, β combination. In this, we utilized the "single long run" described by Goutsias [39] by cycling through the image disregarding the first 1000 iterations and then examining the image generated every tenth iteration thereafter. The number of clusters and cluster size were found for each image and then these values were averaged. Once these functions are found, we can determine the parameter values that match the expected image characteristics. For the purposes of our examples, we assumed two to three clusters on average, with an area of 0.3 cm^2 for each cluster. Using the mesh plots in Fig. 2, we found that the appropriate parameter values are $\alpha = 0.20$ and $\beta = 0.05$.

Due to boundary effects, the average number of clusters and cluster size will vary with different reconstruction regions. Therefore, the plots shown in Fig. 2 and the specific parameter values are included here only as examples. The procedure described here could be repeated for new reconstruction regions. Alternatively, standard parameter estimation methods could be used if suitable training images are available.

Having specified the parameters of the prior on the indicator process $\mathbf{x}$, we proceed with the development of the posterior probability. The source amplitude process, $\mathbf{z}$, is assumed to be a set of independent zero-mean Gaussian random variables with covariance $\mathbf{C}_z$. Assuming the noise process in (1) is

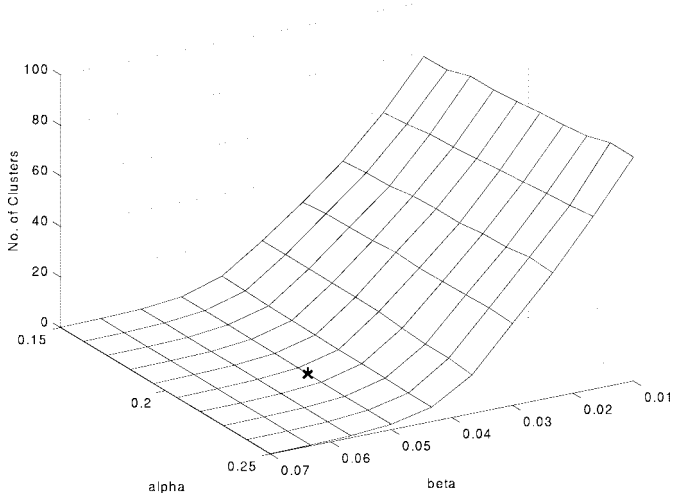

(a)

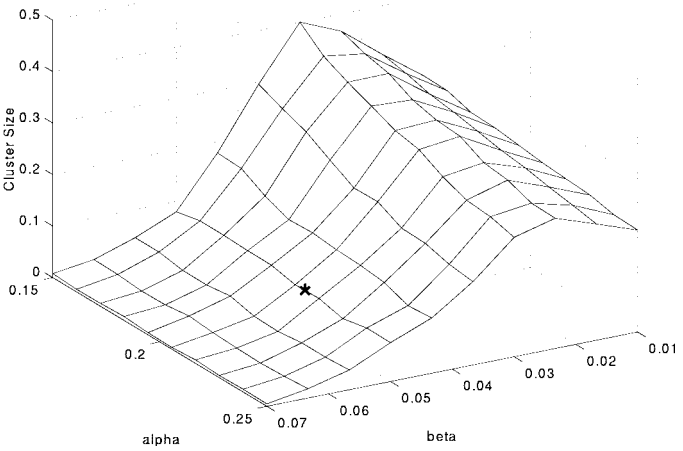

(b)

Fig. 2. Mesh plots showing the average properties for the annular image region in Fig. 1 for $0.15 \leq \alpha \leq 0.25$, $0.01 \leq \beta \leq 0.07$, and $Q = 2.5$. (a) Average number of clusters. (b) Average cluster size (in cm^2). The "*" shows the position of the α, β combination used in subsequent studies.

zero-mean Gaussian with covariance $\mathbf{C}_n$, we can write

$$p(\mathbf{x}, \mathbf{z}|\mathbf{b}) = \frac{1}{Z} \exp\{-U(\mathbf{x}, \mathbf{z}|\mathbf{b})\} \tag{21}$$

where Z is the posterior partition function. The posterior energy function is given by

$$U(\mathbf{x}, \mathbf{z}|\mathbf{b}) = \frac{1}{2}[\mathbf{b} - \mathbf{G}\mathbf{X}\mathbf{z}]^{\mathrm{T}} \mathbf{C}_n^{-1} [\mathbf{b} - \mathbf{G}\mathbf{X}\mathbf{z}] + \frac{1}{2}\mathbf{z}^{\mathrm{T}} \mathbf{C}_z^{-1} \mathbf{z} + V(\mathbf{x}). \tag{22}$$

The MAP estimate is found by maximizing over the log-posterior, or equivalently

$$\mathbf{x}^*, \mathbf{z}^* = \underset{\mathbf{x}, \mathbf{z}}{\arg\min} \; U(\mathbf{x}, \mathbf{z}|\mathbf{b}). \tag{23}$$

The solution to the optimization problem (23) provides our estimate of the neural current sources.

V. Mean Field Annealing

Minimization of $U(\mathbf{x},\mathbf{z}|\mathbf{b})$ is difficult since the optimization must be performed over a mixture of discrete and continuous variables. Since this function is quadratic in the continuous variables, $\mathbf{z}$, we can derive a closed form expression for the optimal $\mathbf{z}$ as a function of any particular indicator process $\mathbf{x}$. i.e. the vector $\mathbf{z}^*(\mathbf{x})$ which minimizes (22) given the binary vector $\mathbf{x}$ is given by [cf. (12)],

$$\mathbf{z}^*(\mathbf{x}) = \mathbf{C}_z\mathbf{X}\mathbf{G}^{\mathrm{T}}(\mathbf{G}\mathbf{X}\mathbf{C}_z\mathbf{X}\mathbf{G}^{\mathrm{T}} + \mathbf{C}_n)^{-1}\mathbf{b}. \tag{24}$$

Substituting $\mathbf{z}^*(\mathbf{x})$ into $U(\mathbf{x},\mathbf{z}|\mathbf{b})$ results in

$$\tilde{U}(\mathbf{x}|\mathbf{b}) = U(\mathbf{x},\mathbf{z}|\mathbf{b})\big|_{\mathbf{z}\,=\,\mathbf{z}^*(\mathbf{x})} \tag{25}$$

which is a Gibbs energy function for the binary density $\tilde{p}(\mathbf{x}|\mathbf{b}) = (1/\tilde{K})\exp\{-\tilde{U}(\mathbf{x}|\mathbf{b})\}$. We can, therefore, first find the optimal indicator process by minimizing $\tilde{U}(\mathbf{x}|\mathbf{b})$, then substitute this result in (24) to obtain the optimal amplitude process.

Coordinate-wise optimization with respect to a collection of binary variables using, for example, iterated conditional modes (ICM) [40], tends to produce rapid convergence to an undesirable local minimum. We have found that to be the case here, and use instead a continuation method based on mean field annealing (MFA) [41].

MFA changes an optimization problem into a series of expected value problems. We form a new density function based on a temperature parameter T

$$\tilde{p}_T(\mathbf{x}|\mathbf{b}) = \frac{1}{K_T}\tilde{p}^{\frac{1}{T}}(\mathbf{x}|\mathbf{b}) = \frac{1}{\tilde{K}_T}\exp\{-\tilde{U}(\mathbf{x}|\mathbf{b})/T\} \tag{26}$$

where $\tilde{K}_T$ is a temperature-dependent normalization parameter. The mean of the newly defined process $\tilde{p}_T(\mathbf{x}|\mathbf{b})$ approaches the mode of $\tilde{p}(\mathbf{x}|\mathbf{b})$ as $T \to 0$ in the following sense.

Theorem: If $\mathbf{x}^*$ is the unique global maximizer of $\tilde{p}(\mathbf{x}|\mathbf{b})$, then

$$\lim_{T\to 0} \quad E_T\{\mathbf{x}|\mathbf{b}\} = \mathbf{x}^* \tag{27}$$

where $E_T\{\mathbf{x}|\mathbf{b}\}$ denotes the expected value of $\mathbf{x}$ with respect to $\tilde{p}_T(\mathbf{x}|\mathbf{b})$

$$E_T\{\mathbf{x}|\mathbf{b}\} = \frac{1}{\tilde{K}_T}\sum_{\mathbf{x}}\mathbf{x}\exp\{-\tilde{U}(\mathbf{x}|\mathbf{b})/T\}. \tag{28}$$

Proof: If we separate $\mathbf{x}^*$ from the summation and multiply the numerator and denominator by $\exp\{\tilde{U}(\mathbf{x}^*|\mathbf{b})/T\}$, we can rewrite this as

$$E_T\{\mathbf{x}|\mathbf{b}\} = \frac{\left(\sum_{\mathbf{x}\neq\mathbf{x}^*}\mathbf{x}\exp\{[\tilde{U}(\mathbf{x}^*|\mathbf{b}) - \tilde{U}(\mathbf{x}|\mathbf{b})]/T\}\right) + \mathbf{x}^*}{\left(\sum_{\mathbf{x}\neq\mathbf{x}^*}\exp\{[\tilde{U}(\mathbf{x}^*|\mathbf{b}) - \tilde{U}(\mathbf{x}|\mathbf{b})]/T\}\right) + 1}. \tag{29}$$

Since $\mathbf{x}^*$ is the unique global maximizer, $\tilde{U}(\mathbf{x}^*|\mathbf{b}) < \tilde{U}(\mathbf{x}|\mathbf{b}) \quad \forall \quad \mathbf{x} \neq \mathbf{x}^*$. Therefore, the summations go to zero as $T \to 0$ and (27) results. Q.E.D.

Using (28) to determine $E_T\{\mathbf{x}|\mathbf{b}\}$ is infeasible due to the large dimensionality and coupling in $\mathbf{x}$. Instead we use a mean field approximation [42] to simplify the computation of the (approximate) mean. Let S represent all elements of the field. For each pixel i we create a univariate energy function $U_i^{\mathrm{mf}}(x_i|\mathbf{b})$, written as

$$U_i^{\mathrm{mf}}(x_i|\mathbf{b}) = \tilde{U}(\mathbf{x}|\mathbf{b})|_{\mathbf{x}_{S-i}\,=\,\bar{\mathbf{x}}_{S-i}} \tag{30}$$

where $\bar{\mathbf{x}}_{S-i}$ denotes the mean of the field restricted on $\{S-i\}$. We define $K_{i,T}^{\mathrm{mf}}$ to be the corresponding mean field local partition function

$$K_{i,T}^{\mathrm{mf}} = \sum_{x_i}\exp\{-U_i^{\mathrm{mf}}(x_i|\mathbf{b})/T\}. \tag{31}$$

We then approximate the joint probability, $\tilde{p}_T(\mathbf{x}|\mathbf{b})$, as the product of independent mean field approximated univariate probabilities

$$p_T^{\mathrm{mf}}(\mathbf{x}|\mathbf{b}) = \prod_i p_T^{\mathrm{mf}}(x_i|\mathbf{b}) = \frac{\exp\{-\sum_i U_i^{\mathrm{mf}}(x_i|\mathbf{b})/T\}}{K_T^{\mathrm{mf}}} \tag{32}$$

where the overall mean field partition function K_T^{mf} is the product of all local mean field partition functions. This mean field approximation effectively replaces the influence of the statistical fluctuations of neighboring sites by their mean values, where the means are computed with respect to the approximated probability $p_T^{\mathrm{mf}}(\mathbf{x}|\mathbf{b})$.

Using this mean field approximation, we can compute $\bar{x}_{i|\mathbf{b}}(T)$, the approximated posterior mean at temperature T and pixel site i, as

$$\bar{x}_{i|\mathbf{b}}(T) = \frac{1}{K_{i,T}^{\mathrm{mf}}}\sum_{x_i\in\{0,1\}} x_i\exp\{-U_i^{\mathrm{mf}}(x_i|\mathbf{b})/T\} \tag{33}$$

$$= \frac{1}{K_{i,T}^{\mathrm{mf}}}\exp\{-U_i^{\mathrm{mf}}(x_i=1|\mathbf{b})/T\}. \tag{34}$$

Note that the mean is computed with respect of the approximation in (32) to the joint density $\tilde{p}_T(\mathbf{x}|\mathbf{b})$ in (26). Substituting $K_{i,T}^{\mathrm{mf}}$ from (31) and dividing numerator and denominator by $\exp\{-U_i^{\mathrm{mf}}(x_i=1|\mathbf{b})/T\}$, we can simplify this to

$$\bar{x}_{i|\mathbf{b}}(T) = \frac{1}{1+\exp\{\frac{\Delta U_{i|\mathbf{b}}^{\mathrm{mf}}}{T}\}} \tag{35}$$

where the difference in energies is given by

$$\Delta U_{i|\mathbf{b}}^{\mathrm{mf}} = U_i^{\mathrm{mf}}(x_i=1|\mathbf{b}) - U_i^{\mathrm{mf}}(x_i=0|\mathbf{b}). \tag{36}$$

Note that to compute the mean of pixel i, we need the mean of all other pixels in the image since the statistical coupling between sites in the original probability is replaced with a coupling through their means. Therefore, the mean field must be computed iteratively. In our work, the algorithm cycles several times through all pixels using (35) to update their mean values.

The temperature parameter T is slowly reduced as the iterations proceed. As $T \to 0$, coordinate-wise updating using the conditional mean reduces to the method of ICM [40]. Therefore, the asymptotic local convergence behavior of MFA is identical to that of ICM. It is easy to show that ICM will converge to a local minimum $\mathbf{x}^*$, i.e., to a point $\mathbf{x}^*$ where $\hat{U}(\mathbf{x}^*|\mathbf{b}) < \hat{U}(\mathbf{x}|\mathbf{b}) \quad \forall \quad \mathbf{x} \in \{0,1\}^N$ such that $\mathbf{x}^*$ and $\mathbf{x}$ differ at no more than one site. The potential advantage of MFA over direct application of ICM is that by using the mean in combination with an annealing schedule, we can slowly approach the solution and hopefully avoid undesirable local minima.

Our algorithm to perform MFA is summarized as follows.

1) Set $T(0)$ and find an arbitrary initialization for $\bar{x}_{j|\mathbf{b}}[0], j = 1 \cdots N$. Set the location of interest $i = 1$ and the iteration number $k = 0$.
2) Use (24) to determine $\mathbf{z}^*(\mathbf{x}[k])$ for $x_i[k] = 0$ and $x_i[k] = 1$, all other $x_j[k]$ set to $\bar{x}_{j|\mathbf{b}}[k], j \neq i$.
3) Use the $\mathbf{z}^*$ vectors to find $U_i^{\mathrm{mf}}(x_i = 1|\mathbf{b})$ and $U_i^{\mathrm{mf}}(x_i = 0|\mathbf{b})$.
4) Use (35) to calculate $\bar{x}_{i|\mathbf{b}}[k]$.
5) Increment i. If $i \leq N$, go back to 2), else go to 6).
6) Increment the iteration number k and decrease $T(k)$, set $i = 1$, and if not converged go to 2).

We have found empirically that a good choice for the annealing schedule $T(k)$ is

$$T(k) = T_0 \exp\{-k/K_{\mathrm{c}}\} \tag{37}$$

where K_{c} is a constant controlling the rate of $T(k)$'s decrease and T_0 is the initial temperature. Bilbro *et al.* [41] find that in MFA, after a certain "critical temperature," all locations in a binary problem move to the binary values without any direction change. They suggest at least 40 iterations to reach this temperature. Hiriyannaiah *et al.* [43] have found the optimal initial temperature is noise dependent and of order σ^2, where σ^2 is the noise variance. They also find that a decrement of 5% or less in the temperature works well as a general annealing schedule. We have found these numbers to be a useful guide.

Note that this algorithm requires that we take the inverse of an $M \times M$ matrix twice in step 2). This can be computationally prohibitive, especially if we have a large number of sensors. To increase the computational speed, we recognize that when we change only one element from its current value to either a zero or a one, we effectively make a rank one update of the matrix $\mathbf{L} = \mathbf{G}\mathbf{X}\mathbf{C}_{\mathrm{z}}\mathbf{X}\mathbf{G}^{\mathrm{T}} + \mathbf{C}_{\mathrm{n}}$ in (24). A fast method for performing the inverse of a rank one updated matrix was proposed by Sherman and Morrison [cf. 27]. The method is based on the property that the new inverse is a rank one update of the previous inverse. This method requires storing the previous $\mathbf{L}^{-1}$, but it reduces the order of computation from M^3 to M^2.

VI. Simulations

We have conducted extensive simulations based on a simplified two-dimensional (2-D) source model with a one-dimensional (1-D) array of 80 sensors. All dipolar sources are constrained to the annular segment of the $x - y$ plane shown in Fig. 3. The distance between source locations was set to 1.5 mm providing an isotropically sampled image grid of 1098 pixels. All dipoles were constrained in orientation perpendicular to the $x - y$ plane. The source images were chosen using stochastic sampling from $p(\mathbf{x})$ with $Q = 2.5, \alpha_i = 0.200, \beta_i = 0.050,$ and $\sigma_i = 10\mathrm{nAm}, \quad i = 1 \cdots N$. The first three parameters were chosen using the method described in Section IV. The fourth parameter, the standard deviation of the dipole moments, reflects the typical activity seen in an evoked response study [7]. We set $\mathbf{C}_{\mathrm{n}}$ to $\nu^2\mathbf{I}$, where ν^2 is the added noise variance which we assume known. For the study with noiseless data, we assumed a small nonzero ν^2 for our likelihood function, comparable to a signal-to-noise ratio (SNR) of 40 dB, to avoid numerical instabilities.

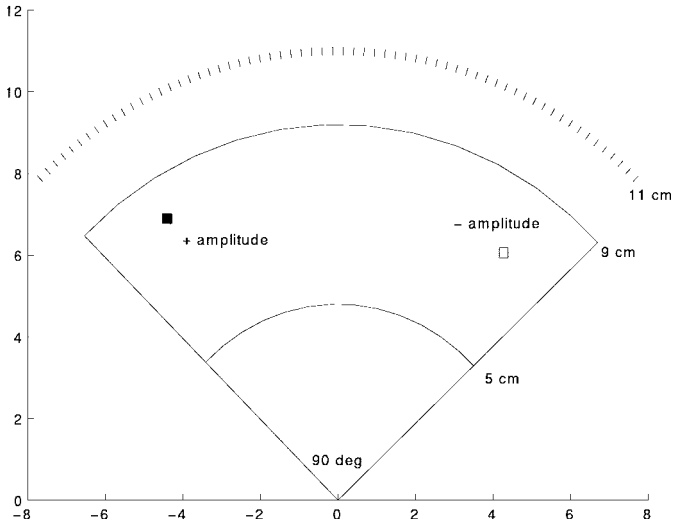

Fig. 3. Sample plot showing the support of the source region (a 90° annulus from 5 to 9 cm) and the locations of the 80 MEG sensors (radial orientation, point measurement). Sources are shown as full boxes (positive amplitude) and empty boxes (negative amplitude), with the area of the box proportional to the magnitude of the source. In the following reconstructions, sources with magnitude less than 1% of the maximum are not included to improve the clarity of the figures.

The results of a representative simulation are shown in Fig. 4 for three scenarios: one noiseless and two with added white Gaussian noise. The percent residual error printed above these images is defined as

$$\left[\frac{(\mathbf{G}\mathbf{y} - \mathbf{b})^{\mathrm{T}}(\mathbf{G}\mathbf{y} - \mathbf{b})}{\mathbf{b}^{\mathrm{T}}\mathbf{b}}\right] \cdot 100\% \tag{38}$$

where $\mathbf{y}$ is the solution shown. SNR is defined as the average signal power at each sensor divided by the noise variance at the sensor. We compared the MAP technique to the four methods described in Sections II and III: standard minimum l_2-norm technique, the normalized minimum norm technique, the LORETA method, and the iteratively reweighted minimum norm technique (FOCUSS).

These results show a wide variation in the characteristics of the solution obtained using different weighting functions. All of the linear minimum norm methods produce results exhibiting a relatively large degree of smoothness. In comparison, both the iteratively reweighted minimum norm and the new Bayesian method produce very sparse solutions.

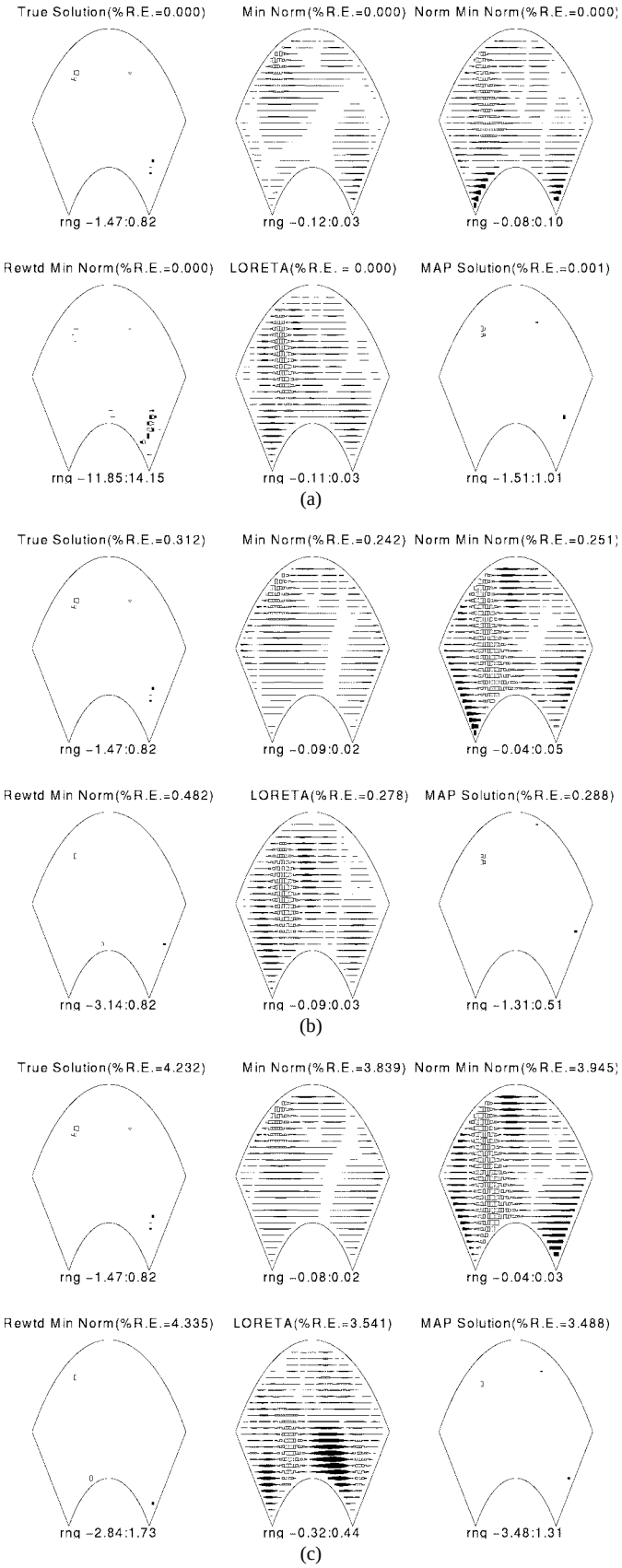

Fig. 4. Sample 2-D simulation with a 1-D sensor array. 80 point measurements, 1,098 point image grid. The percent residual error (% RE) is shown above and the range of source values (in nAm) is shown below each image. Three scenarios are presented: (a) No noise added to the computed data; (b) white Gaussian noise added to the data to achieve an SNR of 20 dB; (c) white Gaussian noise added to the data to achieve an SNR of 8 dB.

Fig. 5. A view from below of the interior of the helmet electronics of the Neuromag-122, showing the configuration of the 61 dual-channel planar first-order gradiometers (Neuromag Ltd., Helsinki, Finland).

For each scenario, all five methods generally give similar residual errors in the fit to the data. In some instances, the iteratively reweighted minimum norm method gives larger errors since there is nothing inherent in the method to limit increases in the error from one iteration to the next. All results can be considered "correct" in the sense that they are configurations that could have produced the observed data. This observation emphasizes the severely under-determined nature of this problem.

We see that as the SNR decreases, performance of all methods deteriorates. In the 20-dB and 8-dB cases, the MAP solution clearly misplaces one of the source clusters, indicating that at these SNR values, it is not possible to resolve between the true source configuration and the MAP reconstruction since both give similar fits to the data and both exhibit the sparse, clustered property preferred by our prior—in fact the MAP reconstruction generally produces a lower posterior energy than the true solution.

Since this is a continuation method, the time required to converge to a solution is an important consideration. Through our rank-one updating techniques, we have managed to keep the time commitment to a minimum. For the simulation shown in Fig. 4(a), using a 100-MHz Indigo-2 SGI workstation, the total CPU time taken to converge was 4 min, 45 s. Note that the time required is a function of the T_0 and K_c parameters from (37). We set $T_0 = 2.0$ and $K_c = 80$ for the MFA in our MAP estimation algorithm.

VII. Phantom Experiments

We have applied the same techniques used in Section VI to experimental phantom data collected with a Neuromag-122 system [7] using the 28-dipole phantom supplied by the manufacturer. The Neuromag-122 system employs 61 dual-channel planar first-order gradiometer units in a helmet-shaped configuration at a radius of 10–11 cm, measuring the magnetic field gradient in two orthogonal tangential directions, for a total of 122 individual sensor measurements. The sensor configuration for a Neuromag-122 is shown in Fig. 5.

The phantom consists of two half circles with a 7-cm radius in the $x-z$ plane and $y-z$ plane, with dipoles in

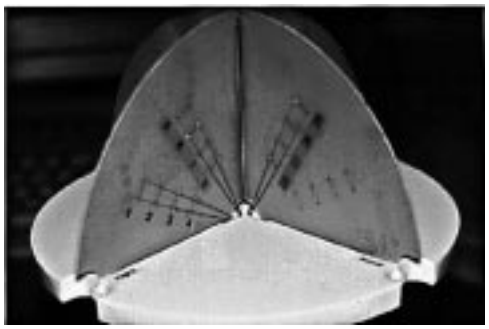

(a)

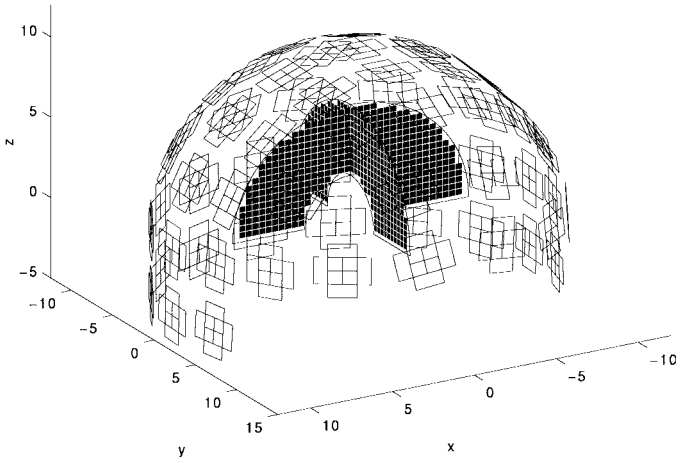

(b)

Fig. 6. (a) The phantom used in the Neuromag-122 experiments consists of 28 tangentially oriented dipoles on two orthogonal planes. These triangular-shaped magnetic dipoles are virtually identical to current dipoles in a conducting solution (see [44] for discussion). (b) Schematic representation of the phantom reconstruction regions (two orthogonal, 180° annular regions) with the locations of the planar gradiometers of the Neuromag-122 system superimposed.

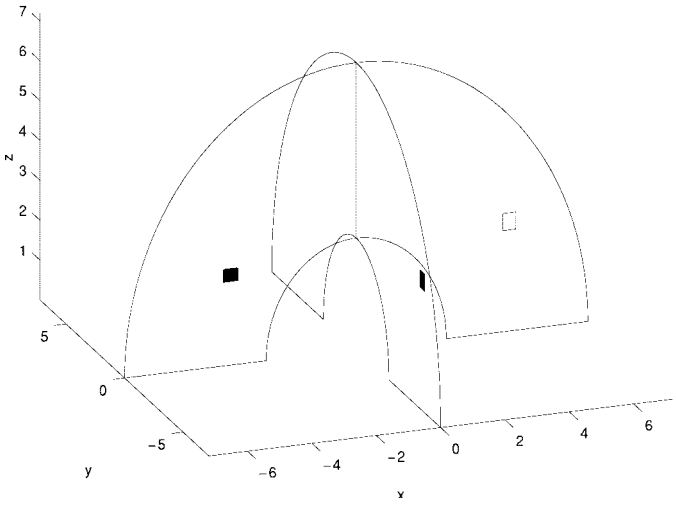

(a)

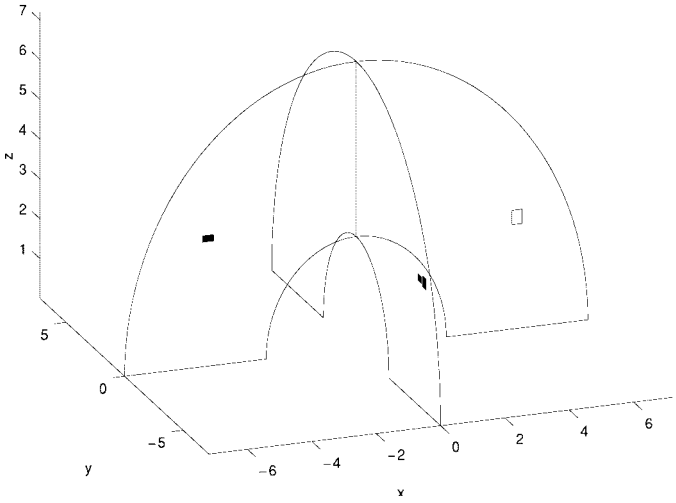

(b)

Fig. 7. Reconstructions from a phantom experiment with three active dipoles. 122 point measurements, 768-point image grid. Colored subject noise was added to the data to achieve an SNR of 15 dB. (a) True configuration of phantom dipoles. (b) MAP Solution.

fixed positions in these planes oriented tangential to the outer edge. The image reconstruction grid consisted of 768 locations spaced 4 mm apart on two 180° annuli, with an inner radius of 3 cm and an outer radius of 7 cm. A photograph of the phantom is shown in Fig. 6(a), and a schematic of the imaging surface with the surrounding sensor elements is shown in Fig. 6(b). The distance between sources and sensors creates a gain matrix which is more poorly conditioned than the one in the previous simulations. This increases the sensitivity to noise of all inverse methods. In all cases, the gain matrix was constructed to include gradiometer effects and nonradial sensor orientations assuming a spherical source volume using the Sarvas approach [4].

The phantom data were collected at high SNR, then scaled to reflect a reasonable evoked field response. We then added data collected in the same system from a passive human subject (100 averages of a prestimulus interval from an evoked response paradigm). This background was added to the phantom data to obtain a specified SNR. Fig. 7 shows the true configuration and the MAP solution plotted as a 2-D projection of the three-dimensional 3-D source distribution. In this example, noise was added equivalent to an SNR of 15 dB. The minimum norm techniques tested on phantom data performed comparably to the simulations in Section VI. The comparison plots are shown in Fig. 8 with high and low SNR. The phantom experiments show that our forward model is accurate and that the MAP technique can also be used effectively to reconstruct sparse sources from real data. We found that colored noise from the human subject was slightly more damaging than white Gaussian noise, since human subject noise tends to be smoother across the sensor array and, therefore, more likely to resemble spurious sources.

VIII. Conclusions

We have developed a Bayesian framework for image estimation from MEG data and described a MAP reconstruction algorithm. In the simulations and phantom studies we have conducted, our MAP solution was generally superior to those obtained using minimum norm methods. However, this is true only when the sources exhibit the sparse focal characteristics on which our method is based. We stress that all of the methods

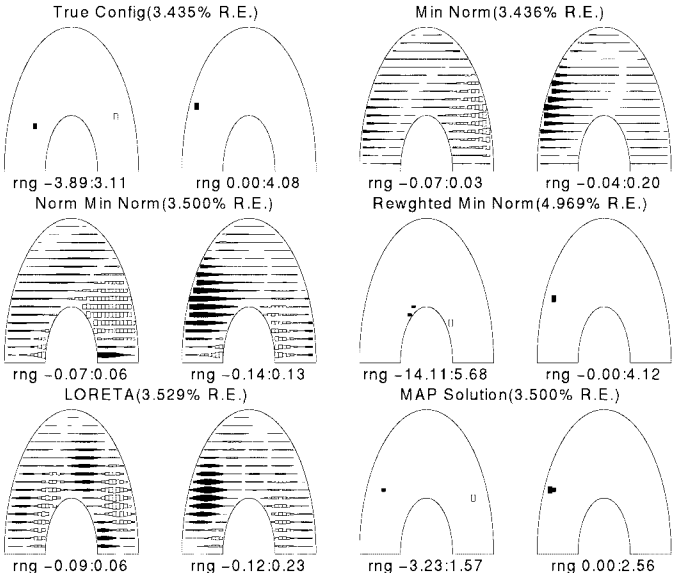

Fig. 8. Sample phantom results with three active dipoles on two orthogonal planes. 122-point measurements, 768-point image grid. Percent residual error (% RE) is shown above and the range of source values (in nAm) is shown below each image. Two scenarios are presented. (a) Colored subject noise added to the data equivalent to an SNR of 15 dB. (b) Colored subject noise added to the data equivalent to an SNR of 10 dB.

provide good fits to the data, and hence are physically (if not physiologically) plausible. This ambiguity is inherent in attempting to infer spatial information from on the order of 100 external sensor measurements. Specific prior information is essential if useful spatial information is to be extracted from the data.

This approach can be extended to include information from other modalities (fMRI or PET) as well as using anatomical MR images to constrain sources to the cortex. The method can also be combined with more accurate forward models, and also used for combined MEG/EEG data. We can also directly extend the model for dynamic imaging by simply replacing each of the amplitude processes, z_i, in our model with a time series model, $z_i(t)$.

The results that we have presented assume sources are constrained to 2-D planes. Future research will focus on sources constrained to a realistic cortical surface. Only then can we begin to establish realistic limits on the ability of MEG to usefully image neural activity.

ACKNOWLEDGMENT

The authors would like to thank J. Lewine of the New Mexico Institute of Neuroimaging, Albuquerque, for providing access to the Neuromag-122 system and data. They would also like to thank C. Aine of the Biophysics group at Los Alamos National Laboratory, Los Alamos, NM, for her prestimulus subject data.

REFERENCES

[1] Y. Okada, "Neurogenesis of evoked magnetic fields," in *Biomagnetism, an Interdisciplinary Approach*, S. J. Williamson *et al.*, Eds. New York: Plenum, 1983, pp. 49–65.
[2] J. C. De Munck, B. W. Van Dijk, and H. Spekreijse, "Mathematical dipoles are adequate to describe realistic generators of human brain activity," *IEEE Trans. Biomed. Eng.*, vol. 35, no. 11, pp. 960–965, 1988.
[3] J. Tripp, "Physical concepts and mathematical models," in *Biomagnetism, an Interdisciplinary Approach*, S. J. Williamson *et al.*, Eds. New York: Plenum, 1983, pp. 101–139.
[4] J. Sarvas, "Basic mathematical and electromagnetic concepts of the biomagnetic inverse problem," *Phys. Med. Biol.*, vol. 32, pp. 11–22, 1987.
[5] J. C. Mosher, R. M. Leahy, and P. S. Lewis, "Matrix kernels for MEG and EEG source localization imaging," in *Proc. IEEE ICASSP*, Detroit, MI, 1995, pp. 2943–2956.
[6] B. N. Cuffin, "A method for localizing EEG sources in realistic head models," *IEEE Trans. Biomed. Eng.*, vol. 42, no. 1, pp. 68–71, 1995.
[7] M. S. Hämäläinen *et al.*, "Magnetoencephalography—Theory, instrumentation, and applications to noninvasive studies of the working human brain," *Rev. Mod. Phys.*, vol. 65, no. 2, pp. 413–497, 1993.
[8] J. C. Mosher, M. E. Spencer, R. M. Leahy, and P. S. Lewis, "Error bounds for EEG and MEG diploe source localization," *Electroenceph. Clin. Neurophysiol.*, vol. 86, pp. 303–321, 1993.
[9] B. N. Cuffin and D. Cohen, "Comparison of the magnetoencephalogram and the electroencephalogram," *Electroenceph. Clin. Neurophysiol.*, vol. 47, pp. 132–146, 1979.
[10] D. Brenner, J. Lipton, and S. J. Williamson, "Somatically evoked magnetic fields of the human brain," *Sci.*, vol. 199, pp. 81–83, 1978.
[11] C. C. Wood, "Application of dipole localization methods to source identification of human evoked potentials," *Ann. NY Acad. Sci.*, vol. 388, pp. 139–155, 1982.
[12] M. Scherg and D. von Cramon, "Two bilateral sources of the late AEP as identified by a spatio-temporal dipole model," *Electroenceph. Clin. Neurophysiol.*, vol. 62, pp. 32–44, 1985.
[13] J. C. Mosher, P. S. Lewis, and R. M. Leahy, "Multiple dipole modeling and localization from spatio-temporal MEG data," *IEEE Trans. Biomed. Eng.*, vol. 39, no. 6, pp. 541–557, 1992.
[14] R. O. Schmidt, "Multiple emitter location and signal parameter estimation," *IEEE Trans. Antennas Propagat.*, vol. 34, pp. 276–280, 1986.
[15] J. P. Wikswo, "Theoretical aspects of the ECG-MCG relationship," in *Biomagnetism, an Interdisciplinary Approach*, S. J. Williamson *et al.*, Eds. New York: Plenum, 1983, pp. 311–326.
[16] R. D. Pascual-Marqui, C. M. Michel, and D. Lehmann, "Low resolution electromagnetic tomography: A new method for localizing electrical activity in the brain," *Int. J. Psycophych.*, vol. 18, pp. 49–65, 1994.
[17] J. Z. Wang, S. J. Williamson, and L. Kaufman, "Magnetic source images determined by a lead-field analysis: The unique minimum-norm least-squares estimation," *IEEE Trans. Biomed. Eng.*, vol. 39, no. 7, pp. 665–675, 1992.
[18] P. C. Hansen, "Regularization tools, a MATLAB package for analysis and solution of discrete ill-posed problems," available in Postscript from http://www. mathworks. com/, 1993.
[19] I. F. Gorodnitsky, J. S. George, and B. D. Rao, "Neuromagnetic source imaging with FOCUSS: a recursive weighted minimum norm

algorithm," *Electroenceph. Clin. Neurophysiol.*, vol. 95, pp. 231–251, 1995.
[20] I. F. Gorodnitsky, B. D. Rao, and J. George, "Source localization in magnetoencephalography using an iterative weighted minimum norm algorithm," in *Proc. Asilomar Conf on Signal System Computation*, Pacific Groove, CA, 1992, pp. 167–171.
[21] R. M Leahy and B. Jeffs, "A DSP algorithm for minimum order solutions from linear constraints," in *Proc. Asilomar Conf on Signal System Computation*, Pacific Groove, CA, 1987, pp. 709–713.
[22] R. M. Leahy, B. Jeffs, and Z. Wu, "A nonlinear simplex algorithm for minimum order solutions," in *Proc. IEEE ICASSP*, New York, 1988, pp. 745–748.
[23] K. Matsuura and Y. Okabe, "Selective minimum-norm solution of the biomagnetic inverse problem," *IEEE Trans. Biomed. Eng.*, vol. 42, no. 6, pp. 608–615, 1995.
[24] K. Matsuura, N. Shimuzu, and Y. Okabe, "Reconstruction of sparse dipole source by a modified SMN method," *Electroenceph. Clin. Neurophysiol.*, to be published.
[25] C. J. Aine, "A conceptual overview and critique of functional neuroimaging techniques in humans—I: MRI/fMRI and PET," *Crit. Rev. Neurobiol.*, vol. 9, nos. 2 and 3, pp. 229–309, 1995.
[26] B. Jeffs, R. Leahy, and M. Singh, "An evaluation of methods for neuromagnetic image reconstruction," *IEEE Trans. Biomed. Eng.*, vol. 34, no. 9, pp. 713–723, 1987.
[27] G. H. Golub and C. F. Van Loan, *Matrix Computations*, 2nd ed. Baltimore, MD: Johns Hopkins Univ. Press, 1989.
[28] A. M. Dale and M. I. Sereno, "Improved localization of cortical activity by combining EEG and MEG with MRI cortical surface reconstruction: A linear approach," *J. Cognitive Neurosci.*, vol. 5, no. 2, pp. 162–176, 1993.
[29] Y. S. Shim and Z. H. Cho, "SVD pseudoinversion image reconstruction," *IEEE Trans Acoust., Speech, Signal Processing*, vol. ASSP-29, no. 4, pp. 904–909, 1981.
[30] P. C. Hansen, "Analysis of discrete ill-posed problems by means of the L-curve," *SIAM Rev.*, vol. 34, pp. 561–580, 1992.
[31] J. O. Berger, *Statistical Decision Theory and Bayesian Analysis*, 2nd ed. New York: Springer-Verlag, 1985.
[32] C. J. S. Clarke, "Probabilistic methods in a biomagnetic inverse problem," *Inverse Problems*, vol. 5, pp. 999–1012, 1989.
[33] P. Hughett, "An optimal constrained linear inverse method for magnetic source imaging," *Ann. Biomed. Eng.*, vol. 23, pp. 506–523, 1995.
[34] A. Tarantola, *Inverse Problem Theory*. New York: Elsevier, 1987.
[35] D. M. Titterington, "Common structure of smoothing techniques in statistics," *Stat. Rev*, vol. 53, no. 2, pp. 141–170, 1985.
[36] A. A. Ionnides, J. P. R. Bolton, and C. J. S. Clarke, "Continuous biomagnetic inverse solutions," *Inverse Problems*, vol. 6, pp. 523–542, 1990.
[37] P. E. Roland, *Brain Activation*. New York: Wiley-Liss, 1993.
[38] S. Geman and D. Geman, "Stochastic relaxation, gibbs distributions, and the bayesian restoration of images," *IEEE Trans Pattern Anal. Machine Intell.*, vol. PAMI-6, pp. 721–741, 1984.
[39] J. Goutsias, "Markov random fields: Interacting particle systems for statistical image modeling and analysis," Johns Hopkins Univ. Tech. Rep. JHU/ECE 96-01, 1996.
[40] J. Besag, "On the statistical analysis of dirty pictures (with discussion)," *J. Roy. Stat. Soc. Ser B*, vol. 48, pp. 259–302, 1986.
[41] G. Bilbro *et al.*, "Optimization by mean field annealing," in *Advances in Neural Information Processing Systems*, D. S. Touretzky, Ed. San Mateo, CA: Morgan-Kaufman, 1989, pp. 91–98.
[42] D. Chandler, *Introduction to Modern Statistical Mechanics*. Oxford, U.K.: Oxford Univ. Press, 1987.
[43] H. P. Hiriyannaiah, G. Bilbro, and W. E. Snyder, "Restoration of piecewise-constant images by mean-field annealing," *Opt. Soc. Amer. J. -A*, vol. 6, no. 12, pp. 1901–1912, 1989.
[44] R. J. Ilmoniemi, M. S. Hämäläinen, and J. Knuutila, "The forward and inverse problems in the spherical model," in Biomagnetism: Applications and Theory. Oxford, UK: Pergamon, 1985, pp. 278–282.